RSC Advances

PAPER

View Article Online
View Journal | View Issue

Open Access Article. Published on 22 August 2025. Downloaded on 3/31/2026 11:29:00 AM.
This article is licensed under a Creative Commons Attribution-NonCommercial 3.0 Unported Licence.

Check for updates

Cite this: *RSC Adv.*, 2025, **15**, 30062

Construction of octanuclear polyoxomolybdenum(v)-based porous materials with lithium additives

Cheng Liu,[a] Zhen-Lang Xie,[b] Xin Dong,[a] Wan-Ting Jin,[c] Yi-Xin Lian[a] and Zhao-Hui Zhou *[a]

Received 29th April 2025
Accepted 4th August 2025

DOI: 10.1039/d5ra03010b

rsc.li/rsc-advances

Crown-ether-like octanuclear polyoxymolybdenum(v) cluster $(NH_4)_4[Mo_8O_8(\mu_2\text{-}OH)_4(\mu_2\text{-}O)_8(dmtrz)_8]\cdot 62.5H_2O$ (dmtrz = 3,5-dimethyltriazole, **1**) was successfully synthesized by a hydrothermal method. Its lithium additives $Li_4[Mo_8O_8(\mu_2\text{-}OH)_4(\mu_2\text{-}O)_8(dmtrz)_8]\cdot 2(Hdmtrz)\cdot 27H_2O$ (**2**), $Li_4[Mo_8O_8(\mu_2\text{-}OH)_4(\mu_2\text{-}O)_8(dmtrz)_8]\cdot 20.5H_2O$ (**3**) and $Li_4[Mo_8O_8(\mu_2\text{-}OH)_4(\mu_2\text{-}O)_8(dmtrz)_8]\cdot 25H_2O$ (**4**) have also been obtained and fully characterized respectively. The lithium cations are in the forms of mononuclear, dinuclear and tetranuclear units. X-ray structural analyses show that polyoxometalate-based materials **1–4** constitute round pores formed by eight molybdenum-oxygen groups connected sequentially with sizes of 4.6 Å. With **1** as the basic framework, **2–4** combine lithium cations in the forms of different hydrates, respectively. In addition, **1** stacked up intermolecularly with pores of sizes 10.0 × 18.0 Å^2, while **4** stacked up inter-molecularly with 6.0 × 4.0 Å^2 in the *a* axis and 8.0 × 5.8 Å^2 in the *c* axis, respectively. The results show that **1** can selectively adsorb CO_2 and O_2, respectively.

Introduction

Various forms of rechargeable batteries have emerged as a promising alternative for conventional energy storage.[1,2] A wide range of materials for lithium-ion batteries have been designed and prepared, which are rechargeable batteries that work primarily by moving lithium cations between the positive and negative electrodes.[3–6] The batteries generally use materials containing lithium as the electrodes. The recycling of waste lithium-ion batteries has become an inevitable choice for recovering valuable resources and protecting the environment.[7–10] It is necessary and practical to capture lithium ions through a number of materials and methods. Moreover, polyoxometalates (POMs) are promising components for energy storage systems;[11] a wide variety of prototype POMs, including Keggin,[12] Anderson,[13] Lindqvist,[14] Dawson,[15] Silverton,[16] and Waugh,[17] are available for the preparation of battery materials. Several polyoxometalates have been utilized in electrode material synthesis, demonstrating suitable cyclic stability and capacity retention in experimental evaluations. Their unique molecular architectures substantially improve Li^+ adsorption kinetics and enable accelerated lithium-ion diffusion.[18–22] Polyoxometalate-based energy storage materials are promising materials to promote the development of novel electrode materials.[23] Despite their many benefits, such as high ionic conductivity and reversible multi-electron transfer capabilities, however, the poor electrical conductivity, low specific surface area, and high solubility of POMs make them challenging for practical applications.[24] Considering these limitations, here we have designed and synthesised polyoxometalate-based metal–organic frameworks (POMOFs). POMOFs are periodic network structures formed by polyoxometalates (POMs) and metal–organic frameworks (MOFs) through covalent bonding or supramolecular forces, and possess the abundant redox-active sites and ordered structures of POMs and MOFs. Five-membered azoles such as imidazole, pyrazole and triazole are well-known building blocks for porous materials. In this study, four octadecanuclear discrete clusters $(NH_4)_4[Mo_8O_8(\mu_2\text{-}OH)_4(\mu_2\text{-}O)_8(dmtrz)_8]\cdot 62.5H_2O$ (**1**), $Li_4[Mo_8O_8(\mu_2\text{-}OH)_4(\mu_2\text{-}O)_8(dmtrz)_8]\cdot 2(Hdmtrz)\cdot 27H_2O$ (**2**), $Li_4[Mo_8O_8(\mu_2\text{-}OH)_4(\mu_2\text{-}O)_8(dmtrz)_8]\cdot 20.5H_2O$ (**3**), $Li_4[Mo_8O_8(\mu_2\text{-}OH)_4(\mu_2\text{-}O)_8(dmtrz)_8]\cdot 25H_2O$ (**4**) were successfully constructed in alkaline aqueous solution by a one-pot method with 3,5-dimethyltriazole. Compound **1** was sequentially linked by eight molybdate groups to form a crown ether-like complex, which provided a platform for Li^+ cations to couple in the form of hydrates *via* intermolecular forces, resulting in compounds **2–4**, where lithium cations were trapped. In addition, the structures of the four compounds can form a ring framework with a diameter of 4.6 Å, respectively, and large pores form by inter-molecule packings.

[a]*Gulei Innovation Institute, Xiamen University, College of Chemistry and Chemical Engineering, Zhangzhou, 363200, Xiamen, 361005, China. E-mail: zhzhou@xmu.edu.cn; Fax: +86 592 2183047; Tel: +86 592 2184531*

[b]*College of Food Science and Engineering, Guangdong Ocean University, Yangjiang, 529500, China*

[c]*College of Chemical and Material Engineering, Quzhou, 324000, China*

© 2025 The Author(s). Published by the Royal Society of Chemistry

Open Access Article. Published on 22 August 2025. Downloaded on 3/31/2026 11:29:00 AM.
This article is licensed under a Creative Commons Attribution-NonCommercial 3.0 Unported Licence.

Gas adsorption experiments have been performed for **1** with the adsorption of carbon dioxide and oxygen.

Results and discussion

Syntheses

Four products were synthesized *via* hydrothermal methods at 80 °C, which provided controlled temperature and pressure conditions for crystallization.[27–30] The pH values of the aqueous solutions play integral roles in the crystallization of **1–4** under mild conditions. The synthesized pH values of **1–4** were 7.2, 9.6, 10.2 and 6.8 respectively, which suggest that the alkaline conditions are more suitable for the syntheses of the porous structures **1–4**. pH modulation with ammonia hydroxide produced compound **1** with a hollow structure in the centre, while compounds **2–4** were obtained by pH modulations with lithium hydroxide as bases. The main structures of **2–4** are similar to that of compound **1**. In addition, the formations of the products depended on the ratio of the reactants, the temperature, and the reducing agent. The ratios of malic acid, $Na_2S_2O_4$ and 3,5-dimethyl-1,2,4-triazole were crucial for the isolations of the Mo8 clusters. The primary function of malic acid may be to stabilize the complexes as templates. In addition, malic acid can be used as a buffer to regulate the pH value of the solutions. Without the addition of malic acid, colorless inorganic salts are formed in the solutions and the yields of the compounds are low. The carboxyl group of malic acid can ionize H^+ and lower the pH value of the solution, while malic acid can form a buffer system with conjugate bases to maintain the pH of the solution stable. The α-hydroxycarboxylic acid structure of malic acid can readily bind to metal ions to form soluble chelates and inhibit metal precipitation. The addition of malic acid facilitates the separation and purification of molybdenum clusters. We report the first incorporation of Li^+ as counterions in crown ether-polyoxometalate (POM) supramolecular architectures. This contrasts with conventional K^+/Na^+ based systems,[25] where large-cavity crown ethers dominate POM assembly. To accommodate the smaller ionic radius of Li^+ (0.76 Å), small-cavity crown ethers such as 12-crown-4 were employed,[26] which have demonstrated stable Li^+ complexation in prior studies but remain unexplored in POM frameworks. This strategy overcomes inherent limitations of traditional K^+ directed systems, diversifying crown ether-POM structural motifs while enabling novel applications in lithium-ion batteries and lithium resource extraction. Future research should focus on synergistic optimization of Li^+ positioning accuracy and structural stability to facilitate practical implementation.

Structural analyses

Tables S1–S12 present the detailed crystallographic data and selected bond distances and angles for **1–4**. Single crystal X-ray diffraction analyses show that the core structures of **1–4** are analogous, featuring crown-ether-like cores with octanuclear molybdenum unit $\{Mo^V{}_8O_8(\mu_2\text{-}O)_8\}$. As shown in Fig. 1a and b, 3,5-dmtrz ligands chelate bidentately with molybdenum atoms

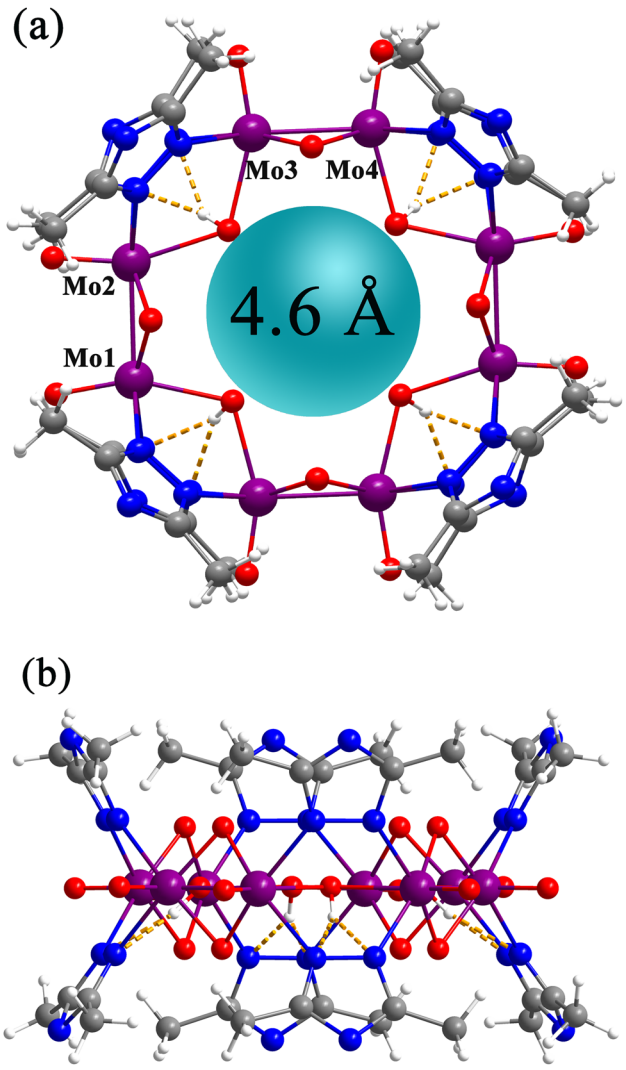

Fig. 1 (a) and (b) Ball-and-stick representations of $(NH_4)_4[Mo_8O_8(\mu_2\text{-}OH)_4(\mu_2\text{-}O)_8(3,5\text{-dmtrz})_8]\cdot 62.5H_2O$ (**1**). (Free and disordered water molecules are omitted for clarity) Color code: molybdenum, violet; oxygen, red; nitrogen, dark blue; carbon, grey; hydrogen, white.

located on either side of the cluster plane. Each central molybdenum atom within the asymmetric unit of complex **1** adopts a distorted octahedral geometry, coordinated by two N atoms from 3,5-dimethyltriazole, three μ_2-O atoms and a terminal oxygen atom. The Mo1 and Mo2 atoms are tightly bound by two μ_2-O groups, which have weak metal–metal bonds, Mo1···Mo2 2.559(3) Å, while the Mo2 and Mo3 atoms [Mo2···Mo3 3.755(3) Å] are bridged by a μ_2-OH and two 3,5-dimethyl-1,2,4-triazoles *via* N atoms. Mo3 and Mo4 are similarly linked by two μ_2-O groups and a weak metal–metal bond between Mo3–Mo4 2.553(4) Å. The whole molecule is a discrete molecular cluster featuring eight metal centers. In the intact pore channel, complex **1** exhibits a pore with an internal diameter of about 4.6 Å. More importantly, the molecule of **1** is linked by π–π conjugation between adjacent triazoles, which increases the stability of the overall structure and creates two additional staggered elliptical pores along the *c*-axis, with the

Open Access Article. Published on 22 August 2025. Downloaded on 3/31/2026 11:29:00 AM.
This article is licensed under a Creative Commons Attribution-NonCommercial 3.0 Unported Licence.

inner walls primarily consisting of coordinated 3,5-dmtrz. As shown in Fig. S1, one of the larger pores is approximately 10 × 18 Å^2 and the other is approximately 3.6 Å, which renders them suitable for applications such as gas adsorption.

The octanuclear molybdenum cluster **2** crystallizes in $P\bar{1}$ space group and consists of a $[Mo_8O_8(\mu_2\text{-OH})_4(\mu_2\text{-O})_8(dmtrz)_8]^{4-}$ unit, lithium cations and free neutral triazole ligands, with 16 water molecules coordinated to the four lithium cations to form two binuclear lithium hydrates. The planar structure of the Mo8 skeleton is in the center, and the lithium hydrates {2,2} are symmetrically arranged on both sides of the Mo8 ring, and the rest of the water molecules are in the form of free crystalline forms. The free neutral ligand 3,5-dimethyl-1,2,4-triazole is attached to the N atoms [N9–N11 2.818(3) Å] of the triazole and the O atoms [N15–O18 2.948(5) Å] of the lithium hydrate, respectively, which are bonded to the Mo8 ring *via* intermolecular hydrogen bonds (Fig. 2).

The octanuclear molybdenum cluster **3** crystallizes in the $P\bar{1}$ space group and consists of a $[Mo_8O_8(\mu_2\text{-OH})_4(\mu_2\text{-O})_8(dmtrz)_8]^{4-}$ unit, lithium cations and two free neutral triazole ligands, in which water molecules coordinate to Li^+ cations to form a dinuclear lithium hydrate and two mononuclear lithium hydrates, respectively. Various Li hydrates are distributed unevenly on both sides of the main structure of the Mo8 ring, forming a {1,3} distribution similar to that of the crystal structure of **2**, as shown in Fig. 3. The remaining water molecules are present as free crystalline water molecules. The three N atoms of the two free neutral ligands interact *via* intermolecular hydrogen bonding with the ligands on the Mo8 ring [N3···N23 2.808(2) Å] and lithium hydrate [N27···O14w 2.834(2) Å, N26···O12w 2.829(3) Å] compounds. The triazole planes of the free ligands between the two adjacent molecules are parallel to each other and the conjugation enhances the stability of the crystal structure.

The octanuclear molybdenum cluster **4** is in a space group *C*2/*c*, consisting of one $[Mo_8O_8(\mu_2\text{-OH})_4(\mu_2\text{-O})_8(dmtrz)_8]^{4-}$, lithium cations, and water molecules. 3,5-dimethyl-1,2,4-triazole ligands are aligned on either side of the metal planes. The anions do not coordinate to the lithium cations, which are coordinated tetrahedrally by four water molecules, of which 12 water molecules bind to lithium cations and form tetranuclear lithium hydrates. The remaining water molecules exist as water molecules of crystallization. The tetranuclear lithium hydrates are composed of two binuclear basic units (symmetry code: 1 − *x*, 2 − *y*, 1 − *z*), whose planes of composition form a dihedral angle of 51.927(3)° with the Mo8 ring plane. The connections of the lithium hydrate to the host structure are attributed to intermolecular hydrogen bonding interactions [O2···O1w 2.739(3), N1···O4w 3.043(7)] as shown in Fig. 4a. Its overall framework is the same as that of **1**, which also has a hollow skeleton of an octanuclear molybdenum-oxygen cluster, while

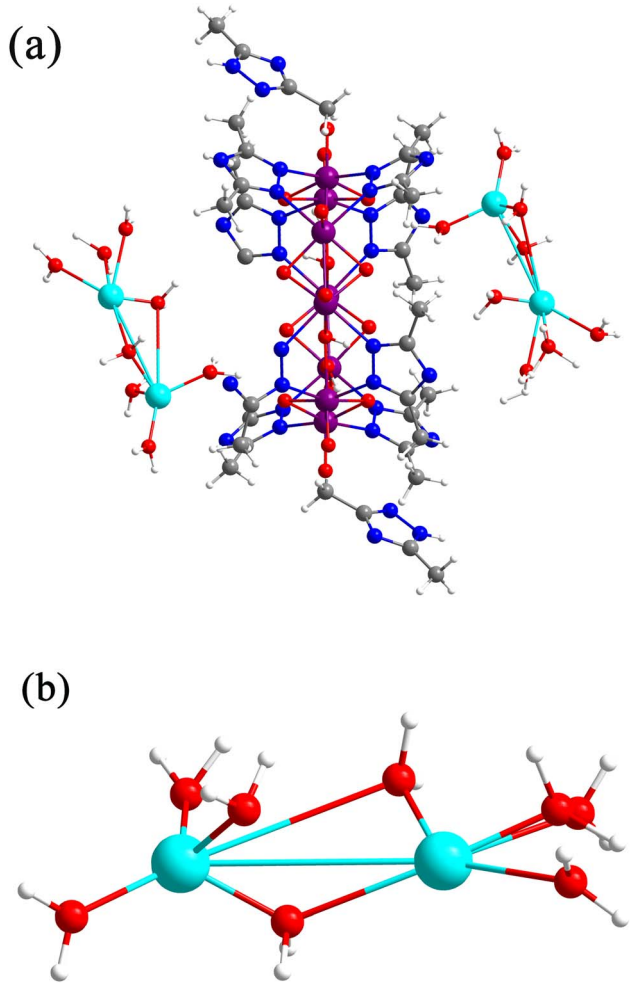

Fig. 2 Ball and-stick representations of: (a) $Li_4[Mo_8O_8(\mu_2\text{-OH})_4(\mu_2\text{-O})_8(3,5\text{-dmtrz})_8]\cdot 2(3\text{-Hdmtrz})\cdot 27H_2O$ (**2**) and (b) $Li_2(\mu\text{-}H_2O)_2(H_2O)_6$ hydrates. Color codes: molybdenum, violet; oxygen, red; nitrogen, dark blue; carbon, grey; hydrogen, white; lithium, wathet.

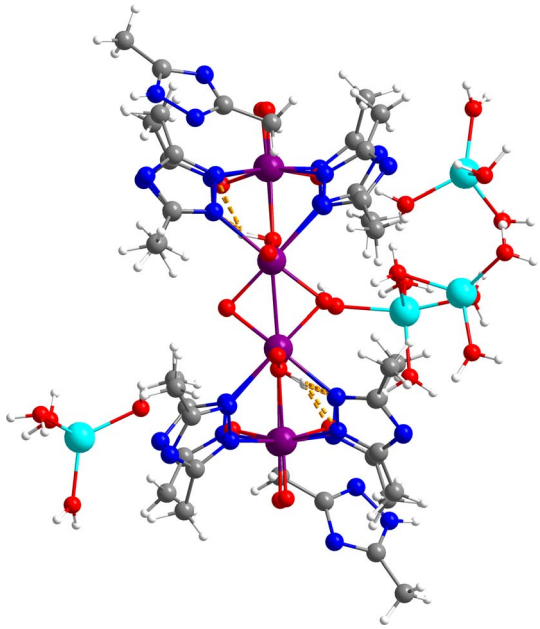

Fig. 3 Ball-and-stick representations of: $Li_4[Mo_8O_8(\mu_2\text{-OH})_4(\mu_2\text{-O})_8(3,5\text{-dmtrz})_8]\cdot 20.5H_2O$ (**3**). Color codes: molybdenum, violet; oxygen, red; nitrogen, dark blue; carbon, grey; hydrogen, white; lithium, wathet.

 © 2025 The Author(s). Published by the Royal Society of Chemistry

Open Access Article. Published on 22 August 2025. Downloaded on 3/31/2026 11:29:00 AM.
This article is licensed under a Creative Commons Attribution-NonCommercial 3.0 Unported Licence.

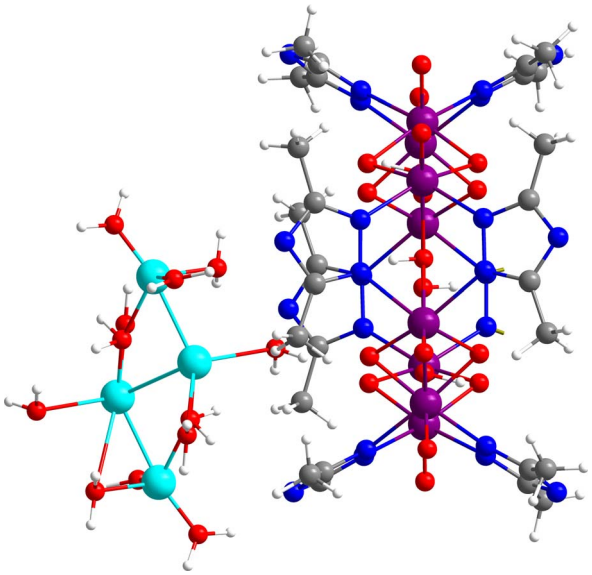

Fig. 4 Ball-and-stick representation of $Li_4[Mo_8O_8(\mu_2\text{-}OH)_4(\mu_2\text{-}O)_8(3,5\text{-dmtrz})_8]\cdot 25H_2O$ (**4**). (Free and disordered water molecules are omitted for clarity) Color code: molybdenum, violet; oxygen, red; nitrogen, blue; carbon, grey; hydrogen, white; lithium cation, wathet. Symmetric code: 1/2 − *x*, 3/2 − *y*, 1 − *z* (Mo), 1 − *x*, 2 − *y*, 3 − *z* (Li).

a tetranuclear lithium hydrate is formed on one side of the Mo8 ring through the hydrogen-bonding interactions involving the triazole ligand, bridging oxygen atoms and water molecules. As shown in Figs. S3 and S4, the crystal structures form elliptical pores with dimensions of 6.0×4.0 Å^2 and 8.0×5.8 Å^2 along the *a* and *c* axes directions by stacking effect.

As shown in Table 1, the average bond lengths between Li atoms and both end-group O and bridging O in mononuclear Li hydrates (**3**, **5–11**), dinuclear Li hydrates (**2**, **12–17**), and tetranuclear Li hydrates (**4**, **18–23**) are presented. The compounds $Li_4[Mo_8O_8(\mu_2\text{-}OH)_4(\mu_2\text{-}O)_8(dmtrz)_8]\cdot 20.5H_2O$ (**3**), $Li_4[Mo_8O_8(\mu_2\text{-}OH)_4(\mu_2\text{-}O)_8(dmtrz)_8]\cdot 2(Hdmtrz)_2\cdot 27H_2O$ (**2**), and $Li_4[Mo_8O_8(\mu_2\text{-}OH)_4(\mu_2\text{-}O)_8(dmtrz)_8]\cdot 25H_2O$ (**4**) have been used for comparisons, respectively. Upon analyzing all the mononuclear Li hydrates in the table, it has been found that the Li–O bond length for the end-group O of compound **2** was 1.969(5) Å, which is significantly larger compared to the end-group O bond lengths of the other Li hydrates. For compound **2**, the average bond length of its end-group O atoms was 2.095(3) Å, and the average bond length for the bridging O atoms was 2.204(1) Å. When compared to other dinuclear Li hydrates, the Li–O bond lengths of both the end-group O and bridging O in compound **2** are relatively large. This may be attributed to the higher density of the electron cloud formed around the O atom by the Mo8 ring and the 3,5-dimethyl-1*H*-1,2,4-triazole ligand, which influences the bond length. Regarding compound **3**, the average bond length of its end-group O atoms is 2.171(3) Å, which is longer than the end-group O bond lengths of the other tetranuclear Li hydrates. In contrast, the average bond length of the bridging O atoms is 1.888(5) Å, which is shorter compared to other tetranuclear Li hydrates. This analysis suggests that the formation of tetranuclear Li in **3** results in a higher degree of electron cloud overlap between the bridging O atom and the two connected Li atoms. This overlap leads to a relatively shorter average bond length for the bridging O atoms in compound **3**.

Gas adsorption properties

To investigate the porous properties of bulk sample **1**, N_2 adsorption–desorption isotherms were recorded at 77 K. As shown in Fig. S5, the isotherm exhibits negligible N_2 uptake.

Table 1 Comparisons of Li–O bond lengths among other crystals with Li hydrates

Nuclearities	Complexes	Li–O$_{terminal}$ (av)/Å	Li–O$_{bridged}$ (av)/Å
Mononuclear	$Li_4[Mo_8O_8(\mu_2\text{-}OH)_4(\mu_2\text{-}O)_8(dmtrz)_8]20.5H_2O$ (**3**)	1.969(5)	
	$[\{Pt(2,2\text{-diMe-}1,3\text{-pd})Cl\}_2(\mu\text{-pz})]Cl_2\cdot 2[Li(H_2O)_4]Cl\cdot 2H_2O$[31]	1.919(3)	
	$[Li(H_2O)_4]_2hmta\cdot ClO_4$[32]	1.940(5)	
	$Li[Ag(Suc)_2]\cdot 4H_2$[33]	1.945(2)	
	$[Li(LAc)(H_2O)_2][Li(H_2O)_4]\cdot H_2O\cdot OC_3H_6$[34]	1.926(2)	
	$Li_4[Fe(C_2O_4)_3]Cl\cdot 9H_2O$[35]	1.925(6)	
	$[Li(H_2O)_4]\cdot hmta\cdot Cl$[36]	1.939(7)	
	$[Li(OH_2)_4]_2[Dy^{III}Cu^{II}{}_2(Me_2pma)_4Cl(H_2O)]\cdot 4H_2O$[37]	1.885(3)	
Dinuclear	$Li_4[Mo_8O_8(\mu_2\text{-}OH)_4(\mu_2\text{-}O)_8(dmtrz)_8]\cdot 2(Hdmtrz)\cdot 27H_2O$ (**2**)	2.095(3)	2.204(1)
	$Li[(C_5H_{10}NS_2)]\cdot 3H_2O$[38]	1.896(2)	2.034(1)
	$[(H_2O)_2Li(OH_2)2Li(OH_2)_2]^{2+}2Cl^-6L$[39]	1.890(2)	2.025(3)
	$[Li(H_2O)_2(\mu_2\text{-}OC_6H_4\text{-}2\text{-}Br)]_2$[40]	1.980(5)	1.932(3)
	$[Li_8(CuL)_4(H_2O)_{10}]\ 2H_2O\ (1.2H_2O)$[41]	1.960(5)	1.978(3)
	$[Li\{(OPPh_2)(SPMe_2)N\}\cdot 2H_2O]_2$[42]	1.957(5)	1.939(2)
	$[Li_2(C_7H_5O_5)_2(H_2O)_8]\cdot 2H_2O$[43]	2.140(3)	2.121(3)
Tetranuclear	$Li_4[Mo_8O_8(\mu_2\text{-}OH)_4(\mu_2\text{-}O)_8(dmtrz)_8]\cdot 25H_2O$ (**4**)	2.171(3)	1.888(5)
	$[Li_2(L_2)0.5(H_2O)_2]n\cdot nH_2O$[44]	2.034(2)	2.123(3)
	$Li_4[C_{13}H_{11}O_2(CH_3CO)_2]_2\cdot nH_2O$[45]	1.983(3)	1.970(5)
	$Li_4(\mu\text{-}O_4\text{-}C_{13}H_7N_2O_2S_2)_4\cdot 4H_2O$[46]	1.943(2)	1.993(4)
	$[Li_2(H_2L_2)(H_2O)_3]n\cdot nH_2O$[47]	2.018(3)	2.106(2)
	$[Li_2(ph\text{-}CF_3\text{-CyOH-4THF})]_2\cdot nH_2O$[48]	1.949(3)	1.948(4)
	$[Li_4(OAr)_4(EGME)_2]\cdot nH_2O$[49]	1.922(4)	1.874(4)

Open Access Article. Published on 22 August 2025. Downloaded on 3/31/2026 11:29:00 AM.
This article is licensed under a Creative Commons Attribution-NonCommercial 3.0 Unported Licence.

Although the channel dimensions of compound 1 (10 Å) significantly exceed the kinetic diameter of N_2 (3.6 Å), only trace adsorption was observed. This phenomenon can be attributed to the exclusively 1D channels along the *c*-axis, with no effective pore connectivity along the *a*- or *b*-axes. Notably, such minimal N_2 adsorption at 77 K has been previously reported for polyoxometalate (POM)-based porous materials,[50,51] primarily due to the hydrophilic nature of POM building units. Nevertheless, considering the abundant active sites within these 1D channels, we further examined the adsorption behaviors of CO_2 and O_2 under varying pressures. The adsorption performances of **1** on small molecular gases such as CO_2, O_2, N_2, CH_4 and H_2 were studied in Fig. 5, using various intrinsic molecular channels. The findings revealed that compound **1** demonstrates pronounced adsorption capabilities for both O_2 and CO_2, while there is no significant absorption for N_2, CH_4 and H_2. Specifically, at 298 K, the adsorption capacity of compound **1** for these gases increases linearly with rising pressure. At 30 bar, the adsorption capacities of compound **1** for O_2 and CO_2 were 25 mg g^{-1} and 8 mg g^{-1}, respectively. Notably, the adsorption amount of O_2 by compound **1** is greater than that of CO_2. The reasons for the adsorption of CO_2 and O_2 by the crystal molecules are analyzed as follows. The CO_2 adsorption process is primarily mediated by electrostatic interaction between the pore surface and CO_2 molecules. Hydrogen atoms of the 3,5-dimethyl-1,2,4-triazole (3,5-dmtrz) ligand within the channels can form weak C–H···O hydrogen bonds with the oxygen atoms of CO_2 molecules.[52,53] Furthermore, the uncoordinated azolate N-donors can also serve as strong adsorption sites.[54] In comparison, the superior O_2 adsorption capacity arises from the oxophilic characteristics of molybdenum centers, which exhibit high affinity for oxygen molecules.[55] Remarkably, powder X-ray diffraction (PXRD) analysis revealed that the characteristic diffraction peaks of sample **1** maintained their positions and intensities after gas adsorption experiments, confirming the preservation of both crystallinity and framework structural integrity.

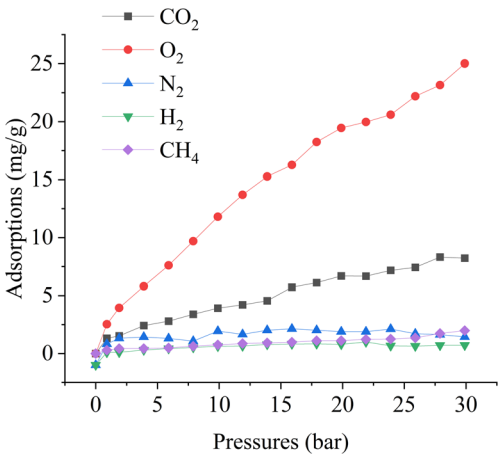

Fig. 5 CO_2, O_2, N_2, CH_4 and H_2 adsorption isotherms of **1** at 298 K and different pressures.

The real adsorption process is complicated and it is not only affected by the pores that we can see intuitively, but also the inner walls of the pores, the sample surfaces and other factors, so we cannot give the most accurate reason for these adsorption behaviors. But the reason for their adsorption to oxygen and carbon dioxide may be related to that the inner walls of the pores are mostly nitrogen and carbon containing ligands, which have good adhesion to CO_2 through hydrogen bonding. Since molybdenum is an oxophilic metal, this suggests that O_2 is highly compressed within the pores here.[56]

Powder X-ray diffraction (PXRD) patterns and thermal and chemical stabilities

The synthesized complexes **1–4** were characterized by X-ray powder diffraction as shown in Fig. S6. By comparing the powder XRD patterns of complexes **1–4** with the simulated curves derived from single crystal structures revealed excellent agreement. It indicates that complexes **1–4** have good phase purities. As shown in Fig. S7, the thermal stability profiles of complexes **1–4** were investigated through thermogravimetric analysis in the temperature range of 0–1000 °C. All complexes exhibited three distinct mass loss stages, though with varying transition temperatures. Specifically, characteristic decomposition events were observed at the following temperatures: complex **1** at 69.1, 319.9, and 421.2 °C; complex **2** at 63.4, 280.0, 320.2, and 414.3 °C; complex **3** at 58.5, 290.6, 419.1, and 799.1 °C; and complex **4** at 65.4, 310.4, and 406.1 °C respectively. In the initial dehydration stage (50–100 °C), all complexes demonstrated lattice water evaporation, evidenced by mass losses of 15.59% (**1**), 16.07% (**2**), 15.90% (**3**), and 11.75% (**4**), corresponding to their respective first weight loss peaks. Subsequent structural decomposition occurred between 280 – 420 °C, with complexes **2** and **4** displaying two consecutive decomposition events in this phase. These transitions are attributed to the sequential breakdown of triazole organic ligands followed by molybdenum-oxygen framework collapse. The final residues across all samples consisted predominantly of thermally stable molybdenum oxide compounds.

Bond-valence calculations and electron paramagnetic resonance (EPR) spectra

Theoretical bond valence calculations (BVS) give the average valences 5.064, 5.056, 4.988 and 5.028 for **1–4** with small errors of +0.064, +0.056, −0.002 and +0.028, respectively. These results reveal that all molybdenum sites are in +5 oxidation states in **1–4**, as described in Table S14. The results are consistent with aforementioned structural analyses and in accordance with the charge balance. And they are further supported by EPR spectroscopy, which detects unpaired electrons and provides detailed information on structure and bonding of paramagnetic species. As shown in Fig. S8, the electron paramagnetic resonance spectra show the pattern of solid anisotropies **1–4**, which is an effective tool for probing unpaired electrons and exploring electronic structure and bonding in paramagnetic metal complexes. The anisotropic contribution is determined by the interaction between the single electron spin and the Mo core (*I*

 © 2025 The Author(s). Published by the Royal Society of Chemistry

Open Access Article. Published on 22 August 2025. Downloaded on 3/31/2026 11:29:00 AM. This article is licensed under a Creative Commons Attribution-NonCommercial 3.0 Unported Licence.

= 5/2). This band shows an $S = 1/2$ signal and weak signals centred on $g = 2.0031$, $g = 2.0037$, $g = 2.0019$ and $g = 2.0026$ for **1–4**, respectively, consistent with the 4 d^1 metal center Mo^{5+}.

IR and solid UV-visible spectra

The infrared spectra of **1–4** were measured in the range of 4000–550 cm^{-1}. Using the Fourier Transform Infrared (FT-IR) technique, the functional groups in complexes **1–4** show specific IR absorption peaks (Fig. S9–S12). Strong absorption bands are observed at around 3340 cm^{-1} for both **1–4**, which represents the stretching vibration ν(OH) of the free water molecules. The absorption peaks in the range 1700–1000 cm^{-1} are attributed to the characteristic vibrations of dmtrz for complexes **1–4** coordinatively, which were compared with IR spectra for the free triazole ligand obtained from the Spectral Database for Organic Compounds (SDBS). In addition, the characteristic vibrational peaks of ν(Mo=O) and ν(Mo–O–Mo) bonds in **1–4** appear in the strong bands around 800–970 and 630–730 cm^{-1}, respectively.

Solid-state UV/Vis spectra were measured for all samples **1–4** at room temperature in Fig. S13. The strong absorptions at 297, 300, 301 and 307 nm for **1–4** are due to the π–π* transitions of triazole ligands. The absorptions in the range 320 – 340 nm represent the charge transition of O → Mo. The strong adsorption bands of **1–4** observed in the range of 400–600 nm were related to the d–d transition of molybdenum(v). The observations are consistent with the orange colors of the samples observed.

Conclusions

In conclusion, four crown-ether-like octanuclear clusters were obtained *via* triazole ligands, molybdate, and Li ions formed different hydrates by strong interactions. Under the control of different pH values and reducing agents, lithium hydrates were further trapped in **2–4**, forming {2,2}, {1,3}, {0,4} hydrates respectively *via* van der Waals forces and intermolecular hydrogen bonds on both sides of the Mo rings. The structural analyses revealed that the Mo8 ring in compounds **1–4** is equipped with internal pores of 4.6 Å in size. This indicates that the complexation of Li ions has no significant effect on the pore size of the main ring. Additionally, due to the stacking effect and the intermolecular interactions between the molecules, compounds **1** and **4** form channels with diameters of 10 × 18 $Å^2$ and 8.0 × 5.8 $Å^2$ (6.0 × 4.0 $Å^2$), respectively. These interactions facilitate the adsorptions of small molecules and gases, as the gas adsorption experiments have demonstrated that POM-based porous materials possess adsorption capacities for small amounts of O_2 and CO_2 gases.

Experimental

Experimental reagents and instruments

$(NH_4)_6Mo_7O_{24}\cdot 4H_2O$, 3,5-dimethyltriazole, hydrazine hydrochloride, malic acid, potassium hydroxide, ammonia solution and sodium hydroxide were used in the experiment, which were purchased from Aladdin's reagent company. These chemicals are of analytical or reagent grade purities. The solutions were used to measure the pH values with a digital PHB-8 meter. By using a Nicolet 380 FT-IR spectrometer, infrared spectra are measured and samples are placed in KBr plates. Solid diffused reflectance is recorded at 298 K by using a Cary 5000 UV-vis spectrophotometer (Varian), with $BaSO_4$ as the white standard. The solid EPR spectra of **1–4** were performed on Bruker EMX-10/12 analysis system with X-band (9.4 GHz) at 110 K. The Netzsch STA 449F5 thermal was used to analyze the TG measurements of **1–4** in the temperature range of 30 to 1000 °C, which were carried out at a heating rate of 10 °C min^{-1} in a pure nitrogen atmosphere. Powder X-ray diffraction (XRD) studies were performed on a Panalytical X'pert PRO diffractometer, scanning from 5° to 50° at a scan speed of 10 °C min^{-1}. Cu Kα radiation, measured at 35 kV and 15 mA, served as the X-ray source. The simulated XRD curves are generated by powder pattern method of Mercury software.

Preparation of $(NH_4)_4[Mo_8O_8(\mu_2\text{-}OH)_4(\mu_2\text{-}O)_8(dmtrz)_8]\cdot 62.5H_2O$ (1)

The synthesis of **1** adopted one-pot procedure. $(NH_4)_6Mo_7O_{24}\cdot 4H_2O$ (0.176 g, 0.14 mmol) and *R*,*S*-malic acid (0.40 g, 3.0 mmol) were dissolved in distilled water (10.0 mL) in sequence. The pH value of the solution was adjusted to 4.0 with ammonia hydroxide. Then, hydrazine hydrochloride (0.136 g, 2.0 mmol) and 3,5-dimethyl-4*H*-1,2,4-triazole (0.097 g, 1.0 mmol) were added to the mixed solution in sequence. After adjusting the pH value of the solution to 9.0 with 5 mol L^{-1} ammonia hydroxide, the mixture was heated in an oven at 80 °C for 24 hours. After cooling to room temperature for 10 hours, the product **1** was obtained after 5 to 6 days. Orange crystals were collected in 68.8% yields (0.486 g) based on molybdenum. Found (calcd for $C_{32}H_{52}Mo_8N_{24}O_{20}$): C, 20.64(20.65); H, 2.79(2.80); N, 18.06(18.05) (%). IR (KBr, cm^{-1}): 3394 vs, 1648 s, 1493 s, 1471 s, 1333 s, 1151 w, 1053 w, 991 w, 947 m, 755 s, 624 w, 571w, 507 w. Solid UV ($BaSO_4$, nm): 233, 294, 350–600.

Preparation of $Li_4[Mo_8O_8(\mu_2\text{-}OH)_4(\mu_2\text{-}O)_8(dmtrz)_8]\cdot 2(Hdmtrz)\cdot 27H_2O$ (2)

The synthesis of **2** adopted one-pot procedure. $(NH_4)_6Mo_7O_{24}\cdot 4H_2O$ (0.176 g, 0.14 mmol) and *R*,*S*-malic acid (0.40 g, 3.0 mmol) were dissolved in distilled water (10.0 mL) in sequence. After adjusted the pH value of the solution to above 4.0 by LiOH to prevent the formation of precipitate. Then, hydrazine hydrochloride (0.136 g, 2 mmol) and 3,5-dimethyl-4*H*-1,2,4-triazole (0.097 g, 1.0 mmol) were added to the mixed solution in sequence. After adjusting the pH value of the solution to 10.0 with solid LiOH, the mixture was heated in an oven at 80 °C for 24 hours. After cooling to room temperature for 10 hours, product **2** was obtained after 5 to 6 days. Orange crystals were collected in 68.8% yields (0.486 g) based on molybdenum. Found (calcd for $C_{32}H_{106}O_{47}N_{24}Mo_8Li_4$): C, 16.17(16.18); H, 4.46(4.47); N, 14.12 (14.10) (%). IR (KBr, cm^{-1}): 3394 vs, 1635 m, 1950 m, 1415 s, 1335 m, 1188 w, 1151 w, 989 w, 944 m, 780 w, 751 s, 700 s, 622 s, 584 s. Solid UV ($BaSO_4$, nm): 227, 291, 350 – 600.

Open Access Article. Published on 22 August 2025. Downloaded on 3/31/2026 11:29:00 AM.
This article is licensed under a Creative Commons Attribution-NonCommercial 3.0 Unported Licence.

Preparation of $Li_4[Mo_8O_8(\mu_2\text{-}OH)_4(\mu_2\text{-}O)_8(dmtrz)_8]\cdot 20.5H_2O$ (3)

The synthesis of **3** also adopted a one-pot procedure. $(NH_4)_6Mo_7O_{24}\cdot 4H_2O$ (0.176 g, 0.14 mmol), *R*,*S*-malic acid (0.40 g, 3.0 mmol), hydrazine hydrochloride (0.136 g, 2.0 mmol) and 3,5-dimethyl-4*H*-1,2,4-triazole (0.097 g, 1.0 mmol) were dissolved in distilled water (10.0 mL) in sequence. The pH value of the solution was adjusted to 4.0 with LiOH. After adjusting the pH of the solution to 9.0 with solid LiOH, the mixture was heated in an oven at 80 °C for 24 hours. After cooling to room temperature for 10 hours, product **3** was obtained after 5 to 6 days. Orange crystals were collected in 68.8% yields (0.486 g) based on molybdenum. Found (calcd for $C_{40}H_{122}O_{47}N_{30}Mo_8Li_4$): C, 18.67(18.68); H, 4.75(4.74); N, 16.35(16.34) (%). IR (KBr, cm^{-1}): 3385 vs, 1630 s, 1562 w, 1490 m, 1413 m, 1372 w, 1337 m, 1148 w, 1057 w, 986 w, 944 m, 751 m, 622 w, 578 w. Solid UV ($BaSO_4$, nm): 231, 298, 350–600.

Preparation of $Li_4[Mo_8O_8(\mu_2\text{-}OH)_4(\mu_2\text{-}O)_8(dmtrz)_8]\cdot 25H_2O$ (4)

The synthesis of **4** also adopted a one-pot procedure. $(NH_4)_6Mo_7O_{24}\cdot 4H_2O$ (0.176 g, 0.14 mmol), *R*,*S*-malic acid (0.40 g, 3.0 mmol), hydrazine hydrochloride (0.136 g, 2.0 mmol) and 3,5-dimethyl-4*H*-1,2,4-triazole (0.097 g, 1.0 mmol) were dissolved in distilled water (10.0 mL) in sequence. The pH value of the solution was adjusted to 4.0 with LiOH. After adjusting the pH of the solution to 11.0 with solid LiOH, the mixture was heated in an oven at 80 °C for 24 hours. After cooling to room temperature for 10 hours, the product **4** were obtained after 5 to 6 days. Orange crystals were collected in 68.8% yields (0.486 g) based on molybdenum. Found (calcd for $C_{40}H_{122}O_{47}N_{30}Mo_8Li_4$): C, 18.67(18.68); H, 4.75(4.74); N, 16.35(16.34) (%). IR (KBr, cm^{-1}): 3398 vs, 1626 s, 1495 s, 1415 s, 1371 w, 1304 s, 1144 s, 1053 w, 995 w, 946 m, 866 w, 784 w, 749 s, 704 w, 620 w. Solid UV ($BaSO_4$, nm): 209, 294, 350 – 600.

Gas adsorption measurements

In the pressure range of 0 to 30 bar, the adsorption capacities of **1** for O_2 and CO_2 are evaluated by a magnetic suspension gravimetric sorption analyzer (ISOSORP-HTGRA) at 298 K. Samples **1** are placed in the sample bucket and then loaded into the adsorption chamber and pressurize continuously with dry gas at 298 K, which the weights of **1** are changed by 70.3 mg, respectively. The sample was then evacuated to remove any traces of water solvents for 7 hours at 393 K, until the weight remained constant. MessPro software tracked the weight change of sample **1** on MSB (RUBOTHERM ISOSORP-HTGRA). Each point of the pressure locations reached adsorption equilibrium after around 40 minutes.

X-ray structural determinations

The X-ray structural analyses of crystals **1–4** were recorded on Rigaku Oxford Diffraction diffractometer using monochromated Cu Kα radiation ($\lambda = 1.5418$ Å) at 298 K. CrysAlisPro was used to process the data for absorption corrections. The structures were solved and improved using the Olex2 and ShelXT programs. The water solvents were masked to remove the strongly disordered water molecules and the possible numbers of solvent molecules were calculated in the accessible void of crystal structures by using the squeeze software. The ShelXT structure solution program was used to solve the structures of **1–4** directly and all non-hydrogen atoms were employed to enhance the structures based on F^2 with the SHELXL-2018/3 program in Olex2. The detailed structural refinements and crystallographic information of **1–4** are recorded in Table S2.

Cyclic voltammograms

Electrochemical characterizations of molybdenum complexes in aqueous media are shown in Fig. S14. The redox characteristics of complexes **1–4** were systematically investigated through cyclic voltammetry (CV) in aqueous 0.20 mol L^{-1} Na_2SO_4 electrolyte. The potential was initially scanned in the anodic direction, followed by reverse scanning through the cathodic reduction region. As depicted in Fig. S13, all complexes exhibited irreversible redox events within the −2.0 to +2.0 V window at 0.1 V s^{-1} scan rate. Notably, anodic peaks observed at 0.414 V (**1**), 0.099 V (**2**), 0.355 V (**3**), and 0.304 V (**4**) could be attributed to the oxidation of reduced Mo^V species. The prominent oxidation features in the 1.2–1.5 V range for all four compounds likely correspond to oxygen evolution through water oxidation, while the cathodic signals between −0.8 and −0.4 V may represent hydrogen evolution *via* water reduction. The reduction peak observed near −1.8 V is a direct electrochemical manifestation of the core process of Mo(VI) reduction, which occurs at that particular potential due to the combined effects of charge compensation, stabilization, and promotion of the porous structures by Li cations.

Author contributions

The manuscript was written through contributions of all authors. All authors have given approval to the final version of the manuscript.

Conflicts of interest

There are no conflicts to declare.

Data availability

CCDC deposited numbers are 2443644–2443647 contain the supplementary crystallographic data for this paper.s

CCDC 2443644–2443647 contain the supplementary crystallographic data for this paper.[57–60]

Polyhedral representations, packing diagrams, powder XRD patterns, IR and solid UV-Vis adsorption spectra, TG-DTG curves, solid EPR spectra of **1–4** at 110 K, crystallographic details, selected bond distances and angles, hydrogen bonds, bond valence calculations for molybdenum atoms. See DOI: **https://doi.org/10.1039/d5ra03010b**.

 © 2025 The Author(s). Published by the Royal Society of Chemistry

Open Access Article. Published on 22 August 2025. Downloaded on 3/31/2026 11:29:00 AM.
This article is licensed under a Creative Commons Attribution-NonCommercial 3.0 Unported Licence.

Acknowledgements

We thank the National Natural Science Foundation of China (22179110) for the generous financial support.

Notes and references

1 J. F. Kurisingal, H. Yun and C. S. Hong, *J. Hazard. Mater.*, 2023, **458**, 131835.
2 H. Wang, D. Yu, C. Kuang, L. Cheng, W. Li, X. Feng, Z. Zhang, X. Zhang and Y. Zhang, *Chem*, 2019, **5**, 313–338.
3 S. Yao, W.-H. Fang, Y. Sun, S.-T. Wang and J. Zhang, *J. Chem. Soc.*, 2021, **143**, 2325–2330.
4 A. Balducci, *Top. Curr. Chem.*, 2017, **375**, 20.
5 J. Dahn, J. Jiang, L. Moshurchak, C. Buhrmester and R. L. Wang, *Electrochem. Soc. Interface*, 2005, **14**, 27.
6 J. B. Goodenough and H. Gao, *Sci. China:Chem.*, 2019, **62**, 1555–1556.
7 X. Bai, Y. Sun, R. He, Z. Liu and J. Pan, *Chem. Eng. J.*, 2024, **500**, 157219.
8 Z. Peng, Q. Lu, Z. Zhu, Y. Zhao and M. Wang, *ACS Sustain. Chem. Eng.*, 2024, **12**, 17249–17262.
9 G. Li, Y. Chen, M. Wu, Y. Xu, X. Li and M. Tian, *Waste Manage.*, 2024, **190**, 141–148.
10 C. Tang, W. Shan, Y. Zheng, L. Zhang, Y. Liu, B. Liao, H. Chen and X. Hou, *Chem. Eng. J.*, 2024, **502**, 157578.
11 Y. Hu, Y. Wang, J. Zhao and L. Chen, *Coord. Chem. Rev.*, 2024, **506**, 215724.
12 H. Wang, S. Hamanaka, Y. Nishimoto, S. Irle, T. Yokoyama, H. Yoshikawa and K. Awaga, *J. Am. Chem. Soc.*, 2012, **134**, 4918–4924.
13 E. F. Wilson, H. N. Miras, M. H. Rosnes and L. Cronin, *Angew. Chem., Int. Ed.*, 2011, **50**, 3720–3724.
14 B. Huang, N. Wang, K. Yang, D. Ke, Y. Fang, X. Hu, B. Wu, Z. Xiao, P. Wu and Y. Wei, *New J. Chem.*, 2018, **42**, 5853–5858.
15 D. Nowicka, N. Vadra, E. Wieczorek-Szweda, V. Patroniak and A. Gorczyński, *Coord. Chem. Rev.*, 2024, **519**, 216091.
16 W. Luo, J. Hu, H. Diao, B. Schwarz, C. Streb and Y.-F. Song, *Angew. Chem., Int. Ed.*, 2017, **56**, 4941–4944.
17 Y. Jia, J. Zhang, Z.-M. Zhang, Q.-Y. Li and E.-B. Wang, *Inorg. Chem. Commun.*, 2014, **43**, 5–9.
18 W. Deng, Z. Zhu, Y. Sun, H. Xu, S. Liu and H. Wen, *Polyoxometalates*, 2024, **3**, 9140071.
19 C. Mu, Z. Du and W. Li, *Polyoxometalates*, 2024, **3**, 9140062.
20 M. Priyadarshini, S. Shanmugan, K. P. Kirubakaran, A. Thomas, M. Prakash and K. Vediappan, *RSC Adv.*, 2021, **11**, 19378–19386.
21 X. Zhang, J. Zhang, G. Wang, C. Zhang, L. Fan, Y. Cao, H. Liu and G. Gao, *Dalton Trans.*, 2025, **54**, 1665–1676.
22 Y. Zhang, Y. Wen, X. Liu, Y. Zhang, X. Jia, W. Li, H. Tang, H. Dou, Y. Li and Y. Zhao, *Dalton Trans.*, 2025, **54**, 7522–7530.
23 Y. Zhang, H. Wang, Q. Yao, F. Yan, C. Cui, M. Sun and H. Zhang, *RSC Adv.*, 2016, **6**, 39618–39626.
24 Y. Ji, L. Huang, J. Hu, C. Streb and Y.-F. Song, *Energy Environ. Sci.*, 2015, **8**, 776–789.
25 R. D. Dai, Z. L. Xie, C. Liu, D. Xin and Z. H. Zhou, *Dalton Trans.*, 2024, **53**, 8980–8987.
26 Z. Lu, Y. Guo, S. Zhang, S. Wu, R. Meng, S. Hong, J. Li, H. Xue, B. Zhang, D. Fan, Y. Zhang, C. Zhang, W. Lv and Q.-H. Yang, *Adv. Mater.*, 2021, **33**, 2101745.
27 M. Shandilya, R. Rai and J. Singh, *Adv. Appl. Ceram.*, 2016, **115**, 354–376.
28 Q. Zhang, S. Yan, X. Yan and Y. Lv, *Sci. Total Environ.*, 2023, **902**, 165944.
29 M. Liu, S. Yang, X. Yang, C.-X. Cui, G. Liu, X. Li, J. He, G. Z. Chen, Q. Xu and G. Zeng, *Nat. Commun.*, 2023, **14**, 3800.
30 R. Shu, L. Nie, Z. Zhao and X. Yang, *J. Mater. Sci. Technol.*, 2024, **175**, 115–124.
31 S. Rajković, M. D. Živković, B. Warżajtis, U. Rychlewska and M. I. Djuran, *Polyhedron*, 2016, **117**, 367–376.
32 R. Kruszynski, T. Sieranski, M. Swiatkowski, M. Zielak, J. Wojciechowski, M. Dzierzawska and E. Czubacka, *J. Chem. Cry.*, 2015, **45**, 484–494.
33 J. Perron and A. L. Beauchamp, *Inorga. Chem.*, 1984, **23**, 2853–2859.
34 D. Specklin, S. Mameri, E. Loukopoulos, G. E. Kostakis and R. Welter, *Polyhedron*, 2015, **100**, 359–372.
35 J. P. Declercq, J. Feneau-Dupont and J. Ladriere, *Polyhedron*, 1993, **12**, 1031–1037.
36 R. Kruszynski, T. Sieranski, A. Bilinska, T. Bernat and E. Czubacka, *Struct. Chem.*, 2012, **23**, 1643–1656.
37 P.-Á. Alejandro, C. Joan, L. Francesc, F.-S. Jesús, A. Donatella and P. Emilio, *C. R. Chim.*, 2019, **22**, 466–475.
38 I. Ymen, *Acta Crystallogr., Sect. C:Struct. Chem.*, 1984, **40**, 241–243.
39 C. L. Raston, C. R. Whitaker and A. H. White, *Aust. J. Chem.*, 1988, **41**, 413–416.
40 T. C. Rosen, K. Kirschbaum and D. M. Giolando, *Inorg. Chim. Acta*, 2005, **358**, 3680–3690.
41 K. F. Konidaris, A. C. Tsipis and G. E. Kostakis, *ChemPlusChem*, 2012, **77**, 354–360.
42 I. Ghesner, C. Palotas, A. Silvestru, C. Silvestru and J. E. Drake, *Polyhedron*, 2001, **20**, 1101–1105.
43 B. F. Abrahams, C. J. Commons, T. A. Hudson, R. Sanchez Arlt, R. Ahl, E. D. Carajias, J. W. K. Chan, Z. Guo, R. E. Hill, A. McGinty, N. L. Peters, J. Y. P. Poon, J. Qu, J. Qu, E. E. Rochette, C. Walkear, H. Wang, H. Wu, C. Xu and J. Zhang, *Acta Crystallogr., Sect. C:Struct. Chem.*, 2022, **78**, 653–670.
44 W. Wan, Z. B. Zhu, L. H. Huo, Z. P. Deng, H. Zhao and S. Gao, *CrystEngComm*, 2012, **14**, 5274–5284.
45 N. A. Khanjin and F. M. Menger, *J. Org. Chem.*, 1997, **62**, 8923–8927.
46 C. S. Smithson, D. J. MacDonald, T. Matt Letvenuk, C. E. Carello, M. Jennings, A. J. Lough, J. Britten, A. Decken and K. E. Preuss, *Dalton Trans.*, 2016, **45**, 9608–9620.
47 Z. Y. Ge, Z. B. Zhu, Z. P. Deng, L. H. Huo and S. Gao, *CrystEngComm*, 2018, **20**, 2968–2979.
48 D. V. Sevenard, O. Kazakova, E. Lork, T. Dülcks, D. L. Chizhov and G. V. Röschenthaler, *J. Mol. Struct.*, 2007, **846**, 87–96.

Open Access Article. Published on 22 August 2025. Downloaded on 3/31/2026 11:29:00 AM.
This article is licensed under a Creative Commons Attribution-NonCommercial 3.0 Unported Licence.

49 R. Petrus, A. Kowaliński and T. Lis, *Dalton Trans.*, 2024, **53**, 7450–7469.
50 E. L. Zhou, C. Qin, P. Huang, X. L. Wang, W. C. Chen, K. Z. Shao and Z.-M. Su, *Chem.–Eur. J.*, 2015, **21**, 11894–11898.
51 Z. K. Zhu, Y. Y. Lin, H. Yu, X. X. Li and S. T. Zheng, *Angew. Chem., Int. Ed.*, 2019, **58**, 16864–16868.
52 R. G. Miller, M. R. Warren, D. R. Allan and S. Brooker, *Inorg. Chem.*, 2020, **59**, 6376–6381.
53 Y. P. Zhao, Y. Li, C. Y. Cui, Y. Xiao, R. Li, S. H. Wang, F. K. Zheng and G. C. Guo, *Inorg. Chem.*, 2016, **55**, 7335–7340.
54 P. Q. Liao, D. D. Zhou, A.-X. Zhu, L. Jiang, R. B. Lin, J. P. Zhang and X. M. Chen, *J. Am. Chem. Soc.*, 2012, **134**, 17380–17383.
55 L. Deng, X. Dong and Z. H. Zhou, *Chem.–Eur. J.*, 2021, **27**, 9643–9653.
56 L. Deng, D. H. Ma, Z. L. Xie, R. Y. Lin and Z. H. Zhou, *Dalton Trans.*, 2023, **52**, 8800–8810.
57 C. Liu, Z. L. Xie, X. Dong, W. T. Jin, Y. X. Lian and Z. H. Zhou, CCDC 2443644: Experimental Crystal Structure Determination, 2025, DOI: **10.5517/ccdc.csd.cc2n0t7r**.
58 C. Liu, Z. L. Xie, X. Dong, W. T. Jin, Y. X. Lian and Z. H. Zhou, CCDC 2443645: Experimental Crystal Structure Determination, 2025, DOI: **10.5517/ccdc.csd.cc2n0t8s**.
59 C. Liu, Z. L. Xie, X. Dong, W. T. Jin, Y. X. Lian and Z . H .Zhou, CCDC 2443646: Experimental Crystal Structure Determination, 2025, DOI: **10.5517/ccdc.csd.cc2n0t9t**.
60 C. Liu, Z. L. Xie, X. Dong, W. T. Jin, Y. X. Lian and Z. H. Zhou, CCDC 2443647: Experimental Crystal Structure Determination, 2025, DOI: **10.5517/ccdc.csd.cc2n0tbv**.

 © 2025 The Author(s). Published by the Royal Society of Chemistry